Ab-Initio Calculations of the Vibrational Properties of Nanostructures

Gabriel Bester and Peng Han

1 Introduction

Colloidal semiconductor nanocluster research is a rapidly growing field driven by the attractive idea to tailor material properties by acting on the morphology of the structures. The modification of the optical properties by merely changing the diameter of colloidal quantum dots is one of the figureheads of nanostructure science [1–3]. It is the intense research effort towards the fabrication of nanostructures with favorable properties that has helped to establish most of the knowledge base we rely on today. Till now, the modification of the electronic and optical properties by changing the size of the nanoclusters are well understood theoretically and well controlled experimentally. One open problem of nanostructure science is the effects of temperature on the electronic and optical properties of nanoclusters and hence their vibrational properties. A theory at $T = 0\,\mathrm{K}$ yields very valuable results to unveil certain aspects of the underlying physics, but to make predictions valid in the real world, where the physical properties such as temperature broadening, quantum coherence dephasing, spin-flip transitions and relaxation of charge carriers are key components [4–6], the effects of vibration and temperature on the dynamical processes must be addressed.

The vibrational properties such as the phonon density of states (DOS) and dispersion of bulk semiconductors have been calculated with great accuracy using ab initio density functional perturbation theory (DFPT) since the end of the last century [7]. After the successful applications of DFPT on bulk phonon eigenmodes, ab initio studies on the vibrational properties of semiconductor nanostructures such as fullerenes, nanowires, nanotubes, and nanoclusters with small sizes have been performed [8–10]. However, an accurate density functional theory (DFT) study on the vibrational properties of nanoclusters with the experimentally relevant size of

G.Bester (✉) · P. Han
Max-Planck-Institut für Festkörperforschung, Stuttgart, Germany
e-mail: g.bester@fkf.mpg.de; p.han@fkf.mpg.de

W.E. Nagel et al. (eds.), *High Performance Computing in Science and Engineering '12*,
DOI 10.1007/978-3-642-33374-3_13,

few nm diameter has not been reported until now due to the high computational demand.

With the computational facility available at the Höchst Leistungs Rechenzentrum Stuttgart (HLRS), we have recently calculated confinement and surface effects on the vibrational properties of colloidal semiconductor nanoclusters based on first-principles DFT. We describe how the molecular-type vibrations, such as surface-optical, surface-acoustic, and coherent acoustic modes, coexist and interact with bulk-type vibrations, such as longitudinal and transverse acoustic (LA, TA) and optical (LO, TO) modes. We could link the vibrational properties to structural changes induced by the surface and highlight the qualitative difference between III–Vs and II–VIs semiconductor nanoclusters [11]. We describe the specific heat of nanoclusters at low temperature and link the thermodynamic properties to the low frequency vibrational modes and the surface structure. We suggest that the low temperature specific heat should be a promising avenue to study the surface properties of nanoclusters. Since nanoclusters are believed to have only a certain fraction of their surface atoms directly passivated by ligand atoms, we study the effects of the removal of passivant and the reconstruction of the surface on the vibrational properties. We attribute the strong modification of the vibrational properties to the transformation from sp^3 to sp^2 bonds.

2 Computational Methods

2.1 Research Methodology

A detailed review on density functional theory applied to lattice-dynamical calculations has been given elsewhere [7]. Here, we briefly outline our research methodology. Based on the adiabatic approximation (Born-Oppenheimer approximation), the lattice-dynamical properties of a system are given by

$$[-\sum_I \frac{\hbar^2}{2M_I}\frac{\partial^2}{\partial \mathbf{R}_I^2} + E(\{\mathbf{R}\})]\Phi(\{\mathbf{R}\}) = \varepsilon\Phi(\{\mathbf{R}\}) \tag{1}$$

where $\mathbf{R}_I$ is the coordinate of atom I, M_I its mass, $\{\mathbf{R}\}$ the nuclei configuration given as a set of atomic positions, $\hbar$ the Planck constant, ε and $\Phi(\{\mathbf{R}\})$ the eigenvalue and eigenvector of the lattice vibrations, respectively. $E(\{\mathbf{R}\})$ is the ground state energy of the system, which is determined by the many body Hamiltonian

$$H_{BO}(\{\mathbf{R}\}) = -\frac{\hbar^2}{2m}\sum_i \frac{\partial^2}{\partial \mathbf{r}_i^2} + \frac{e^2}{2}\sum_{i\neq j}\frac{1}{|\mathbf{r}_i - \mathbf{r}_j|} - V_R(\mathbf{r}) + V_N(\{\mathbf{R}\}) \tag{2}$$

where m is the mass of the electron, e the electron charge, and $\mathbf{r}_i$ the coordinate of electron i. The electron-nucleus interaction potential $V_R(\mathbf{r})$ is given by

$$V_R(\mathbf{r}) = -\sum_{i,I} \frac{Z_I e^2}{|\mathbf{r}_i - \mathbf{R}_I|} \tag{3}$$

with Z_I represents the charge of the nucleus I. The electrostatic interaction potential $V_N(\{\mathbf{R}\})$ is written as

$$V_N(\{\mathbf{R}\}) = \frac{e^2}{2} \sum_{I \neq J} \frac{Z_I Z_J}{|\mathbf{R}_I - \mathbf{R}_J|}. \tag{4}$$

Based on the Hellmann-Feynmann theorem, the force acting on the nucleus I is

$$F_I = -\frac{\partial E(\{\mathbf{R}\})}{\partial \mathbf{R}_I} = -\langle \Psi(\mathbf{r}, \{\mathbf{R}\}) | \frac{\partial H_{BO}(\{\mathbf{R}\})}{\partial \mathbf{R}_I} | \Psi(\mathbf{r}, \{\mathbf{R}\}) \rangle \tag{5}$$

and the force constant matrix elements are

$$\frac{\partial^2 E(\{\mathbf{R}\})}{\partial \mathbf{R}_I \partial \mathbf{R}_J} = \int \frac{\partial \rho_R(\mathbf{r})}{\partial \mathbf{R}_J} \frac{\partial V_R(\mathbf{r})}{\partial \mathbf{R}_I} dr + \int \rho_R(\mathbf{r}) \frac{\partial^2 V_R(\mathbf{r})}{\partial \mathbf{R}_I \partial \mathbf{R}_J} d\mathbf{r} + \frac{\partial^2 V_N(\{\mathbf{R}\})}{\partial \mathbf{R}_I \partial \mathbf{R}_J} \tag{6}$$

where $\Psi(\mathbf{r}, \{\mathbf{R}\})$ is the electronic ground-state wave function and $\rho_R(\mathbf{r})$ the electron charge density for the nuclei configuration $\{\mathbf{R}\}$. The charge density $\rho_R(\mathbf{r})$ is obtained by mapping the problem onto a set of one-particle equations (Kohn-Sham equations):

$$[-\frac{\hbar^2}{2m} \frac{\partial^2}{\partial \mathbf{r}^2} + V_R(\mathbf{r}) + e^2 \int \frac{\rho_R(\mathbf{r}')}{|\mathbf{r} - \mathbf{r}'|} d\mathbf{r}' + \frac{\delta E_{xc}}{\delta \rho_R(\mathbf{r})}] \psi_n(\mathbf{r}) = \epsilon_n \psi_n(\mathbf{r}) \tag{7}$$

and

$$\rho_R(\mathbf{r}) = 2 \sum_{n=1}^{N/2} |\psi_n(\mathbf{r})|^2 \tag{8}$$

where δE_{xc} is the exchange-correlation energy, ϵ_n and $\psi_n(\mathbf{r})$ are the eigen energy and wave function of the electronic states, respectively.

Based on the harmonic approximation of lattice dynamics, the frequencies ω and the corresponding eigenmodes $\mathbf{u}_I$ are obtained by solving the eigenvalue equation

$$\sum_J \frac{1}{\sqrt{M_I M_J}} \frac{\partial^2 E(\{\mathbf{R}\})}{\partial \mathbf{R}_I \partial \mathbf{R}_J} \mathbf{u}_J = \omega^2 \mathbf{u}_I. \tag{9}$$

To analyze the eigenmodes in terms of core and surface contributions, we calculate the projection coefficients

$$\alpha^{\nu}_{c,s,p} = \frac{\sum_{I}^{(N_c,N_s,N_p)} |\mathbf{X}^{\nu}(I)|^2}{\sum_{I=1}^{N} |\mathbf{X}^{\nu}(I)|^2}, \tag{10}$$

where, N_c, N_s, N_p and N are the core, surface, passivant, and total number of atoms, $\mathbf{X}^{\nu}(I)$ represents the three components that belong to atom I from the $3N$-component eigenvector. We define the surface atoms as the atoms belonging to the outermost seven layers of the cluster (around 3 Å thick). From the phonon DOS $D(\omega)$ we obtain the specific heat according to:

$$C_v(T) = N_A k_B \int_0^{\infty} \left(\frac{\hbar\omega}{k_B T}\right)^2 \frac{e^{\hbar\omega/k_B T}}{(e^{\hbar\omega/k_B T} - 1)^2} D(\omega) d\omega. \tag{11}$$

2.2 Computational Details

The nanoclusters we studied are constructed by cutting a sphere, centered on a cation with T_d point group symmetry, from the zinc blende bulk structure and removing the surface atoms having only one nearest-neighbor bond. The surface dangling bonds are terminated by pseudohydrogen atoms H* with a fractional charge of 1/2, 3/4, 5/4, and 3/2 for group VI, V, III, and II atoms, respectively. The calculations are performed using the local-density approximation (LDA), Trouiller-Martin norm-conserving pseudopotentials with an energy cutoff of 30 Ry for III–Vs and 40 Ry for II–VIs.

The geometry relaxation is performed using the Broyden-Fletcher-Goldfarb-Shano (BFGS) procedure for the optimization of the ionic positions. The forces are minimized to less than 3×10^{-6} a.u. (5×10^{-4} a.u.) under constrained symmetry for the passivated (unpassivated) nanoclusters. With the optimized geometry, the dynamical matrix elements $\frac{\partial^2 E(\{\mathbf{R}\})}{\partial \mathbf{R}_I \partial \mathbf{R}_J}$ are obtained by solving Eq. (6). In the calculation, the charge density $\rho_R(\mathbf{r})$ are obtained by solving the Kohn-Sham equation self-consistently and the values of $\frac{\partial \rho_R(\mathbf{r})}{\partial \mathbf{R}_J}$ are calculated using a finite difference approach. In principle we need $3N$ atomic displacements to obtain all the elements of the dynamical matrix (N being the number of atoms). In practice we calculate a significantly lower number of displacements ($3N/24$) and use the symmetry elements of the point group to deduce the missing elements. This is a key points to be able to treat these large structures.

All the calculations are performed with the CPMD code package developed at the Max Planck Institute in Stuttgart and at IBM in Zürich [12]. The CPMD code is a high performance parallelized plane wave/pseudopotential implementation of DFT. It offers, at the moment, the best scaling among the DFT codes using a hybrid scheme of MPI and OpenMP.

In this project, all the calculations were carried out on the NEC Nehalem Cluster at HLRS with 2.8 GHz and 12 GB memory per nodes, and infiniband interconnects.

The details of the scaling behavior and the performance per CPU for CPMD code have been given elsewhere [13].

3 Results

3.1 Confinement Effects on Vibrational Properties

We have calculated the vibrational properties for a total of 23 nanoclusters made of InP, InAs, GaP, GaAs, CdS, CdSe, and CdTe. The wave function of the lowest unoccupied molecular orbital (LUMO) state for $Ga_{531}As_{532}H^{*}_{412}$ nanocluster with isosurface corresponding to 75 % of the maximum value are presented in Fig. 1. In this report, we extract the essence of these calculations and select representative results. The vibrational DOS of InP and CdS nanoclusters along with the bulk phonon DOS are plotted with a broadening of 0.8 cm^{-1} in Fig. 2. Although formally TA, LA, and TO, LO phonon modes cease to exist in a nanocluster, the comparison with the bulk phonon DOS in Fig. 2e, j reveals an obvious bulk parentage. From Fig. 2, we see that: (i) The III–V (InP) nanoclusters show a blueshift of LO-, TO-, and LA-derived cluster modes with decreasing size while this blueshift cannot be found in II–VIs (CdS). (ii) The surface modes tend to completely fill the acoustic-optic phonon gap in II–VIs but not for III–Vs. (iii) The "broadening" of the bulk-like optical phonon branches induced by the confinement is larger for II–VIs than for III–Vs.

These three effects can be understood from the geometry of the relaxed nanoclusters. We plot the nearest-neighbor distances of relaxed III–Vs and II–VIs nanoclusters as a function of the distance of the respective bond to the cluster center in Fig. 3. From this figure, we see that the bond length at the dot center is reduced through the presence of the surface in all cases. The bond length distribution of III–Vs and II–VIs exhibits qualitative differences. For III–Vs, the surface shells show a successive reduction of bond length, going outward, while II–VIs show a large bond length distribution. The overall reduction of bond length in III–Vs along with the positive Grüneisen parameters explains the blueshift of the LO-, TO-, and LA-derived cluster modes. The lack of shift in the TA modes stems from the small negative Grüneisen parameter for this branch. Moreover, we attribute the broadening of optical branches and the filling of the phonon-gap in II–VIs to the results of the large bond length distribution.

After discussing the confinement effects on the high frequency vibrational modes, we now focus on the low frequency modes. In Fig. 4, we plot the size-dependent lowest frequencies $f_{min} = v/4R$ calculated from the longitudinal and transverse speed of sound v and cluster radius R as solid and dashed curves. The circles and the crosses are the lowest core and surface acoustic modes obtained from the DFT calculations. We see that the lowest core modes follow closely the analytic $1/R$ dependence while the surface acoustic modes are strongly affected

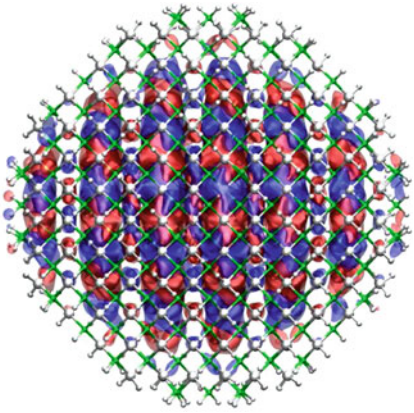

Fig. 1 The wave function of the lowest unoccupied molecular orbit (LUMO) state for a $Ga_{531}As_{532}H^{*}_{412}$ nanocluster with isosurface corresponding to 75 % of the maximum value. The colors *blue* and *red* give the phase of the wave functions

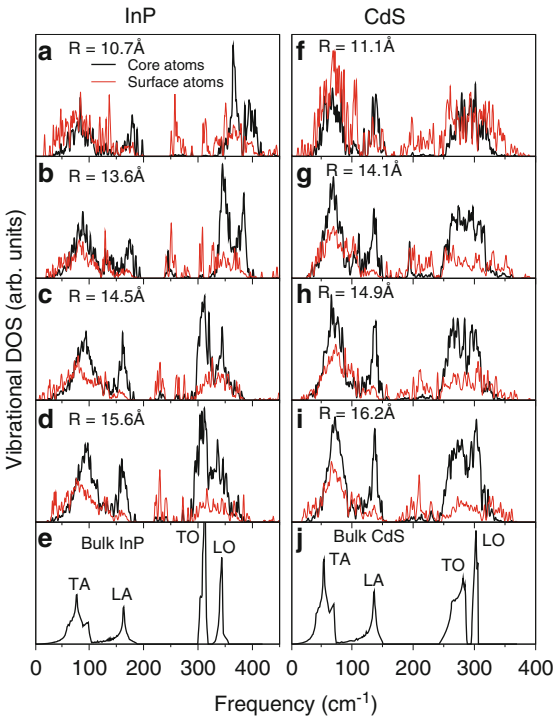

Fig. 2 Vibrational density of states (DOS) contributed by core atoms (*black*) and surface atoms (*red*) for (**a**)–(**d**) InP clusters, (**e**) bulk InP, (**f**)–(**i**) CdS clusters, and (**j**) bulk CdS

by the morphology of the surface and are not monotonous with cluster size. Another important type of vibrational modes are the so-called *coherent acoustic modes*, in which all the atoms vibrate in phase. The coherent phonon modes have been observed with Ramans spectroscopy, far-infrared absorption spectroscopy, and resonant high-resolution photoluminescence spectroscopy, and are now the center of

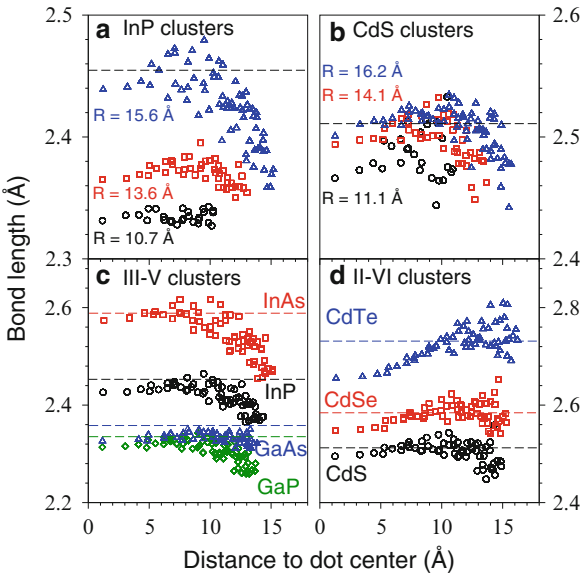

Fig. 3 Bond-length distribution as a function of their distance to the dot center for (**a**) InP, (**b**) CdS, (**c**) III–Vs, and (**d**) II–VIs. LDA bulk bond lengths are given as *dashed lines*

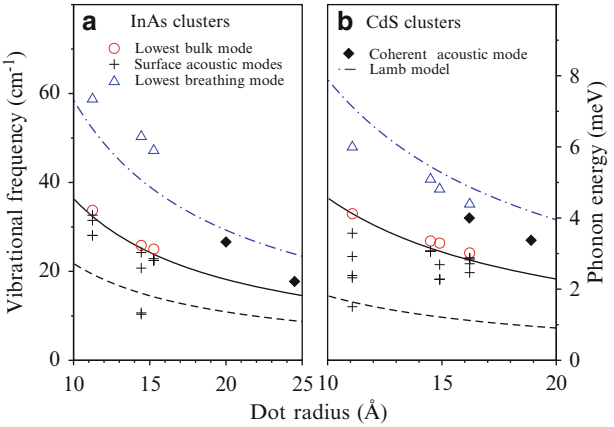

Fig. 4 Size-dependent low frequency vibrational modes for (**a**) InAs and (**b**) CdS. Lowest modes with bulk character (*circles*), surface acoustic modes (*crosses*), lowest breathing modes (*triangles*), and experimental results (Oron et al. [14] and Saviot et al. [18]) for the coherent acoustic modes (*diamonds*). Lowest spheroidal mode according to the Lamb model (*dashed-dotted line*), according to the confined bulk model using the sound velocity of the TA- (*solid lines*) and LA-branch (*dashed lines*)

attention when the manipulation of spins and the spin dephasing is investigated [14–16]. We plot our results as triangles along with the experimental data as diamonds and the results from the Lamb model as dashed-dotted line. Our results are in good agreement with the experimental results (although our clusters sizes are still

somewhat smaller than experiment in the case of InAs) and with the simple Lamb model.

3.2 Passivated versus Unpassivated Nanoclusters

In the real world applications, the nanoclusters are believed to have only a certain fraction of their surface atoms directly passivated by ligand atoms [17]. Thus, we studied an extreme situation where the nanoclusters are unpassivated [19]. In Fig. 5, we compare the vibrational DOS of a fully passivated with geometry optimization (a), an unpassivated nanocluster without (b) and with (c) geometry relaxation. By removing the passivants while frozening the atomic positions, we effectively create dangling bonds in the sp^3 hybrid orbitals. In this frozen geometry, the orbitals cannot redistribute effectively and the bonds close to the surface are weakened. This leads to the red shift of the modes with surface character. Once the geometry is optimized, the dangling bonds tend to transform from sp^3 to sp^2 hybrid orbitals and strengthen. This leads to a blue shift of vibrational modes with a magnitude even greater than the fully passivated cluster and in general a "broadened" vibrational DOS. To understand this effect, we plot in Fig. 6 the relaxed unpassivated cluster (a) and the nearest neighbor distances of a relaxed passivated and a relaxed unpassivated InP nanocluster as a function of the distance of the respective bond to the cluster center (b). From Fig. 6b, we see that the bond length reduction close to the surface is more significant in the case of the unpassivated cluster and this results in the blue shift. Moreover, we can also find that the variation in bond lengths is significantly larger in the unpassivated cluster, which leads to the broadening of the vibrational DOS.

3.3 Thermodynamic Properties

Following the discussion on the vibrational properties, we now turn to the thermodynamic properties of nanoclusters. The vibrational specific heat $C_v(T)$ is calculated using Eq. (11) with the vibrational DOS from DFT computations. Different aspects of the results are summarized in Fig. 7.

In Fig. 7a, we plot $C_v(T)/T$ for CdSeH* nanoclusters with different size as a function of T^2. With this choice of axis, the Debye T^3 regime would appear linear. We identify two distinct regions, *region 1* below $24\,\mathrm{K}^2$ and *region 2* above this temperature. In region 1, $C_v(T)/T$ shows a strongly non-linear dependence and it converts to a nearly linear behavior in region 2. Most surprising is that we find the smaller nanocluster has a larger specific heat than the larger ones. To understand these behaviors, we plot in Fig. 7b the low frequency vibrational spectrum along with the percentage of surface character. The temperature region 1 roughly corresponds to the frequency region below $30\,\mathrm{cm}^{-1}$ in (b), and the small

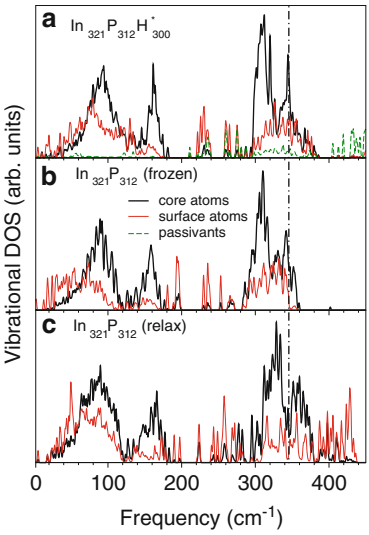

Fig. 5 Vibrational DOS of InP nanoclusters with (**a**) passivant, (**b**) unpassivated without relaxation and (**c**) unpassivated with relaxation

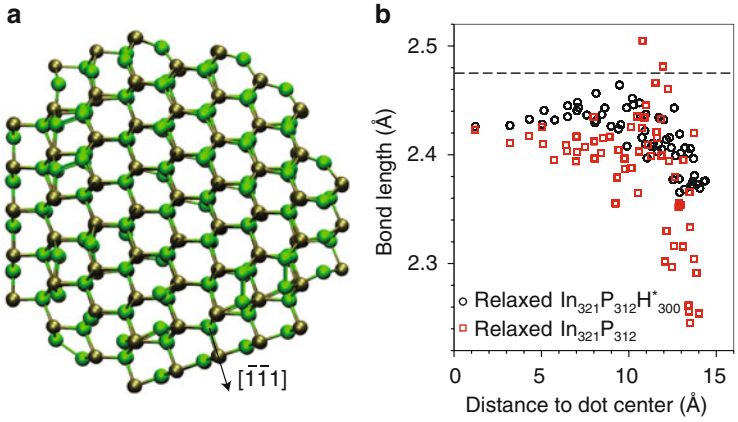

Fig. 6 (**a**) Relaxed geometry of un-passivated $In_{321}P_{312}$ nanoclusters, (**b**) Bond length distribution as a function of their distance to the dot center for $In_{321}P_{312}H^{*}_{300}$. The LDA bulk bond length is given as *dashed lines*

nanoclusters have more vibrational modes (higher vibrational DOS) than the larger ones in this frequency region and these modes have surface character. We can see that the surface modes move up in frequency with increasing cluster size and attribute this effect to the atomic configuration on a curved surface. As depicted in the inset of Fig. 7a, the stronger curvature of smaller dots leads to an "open" surface that allows for softer surface modes. From Fig. 7b, we see that the vibrational modes with core characters contribute to the specific heat when the temperature arrives into region 2. These vibrational modes show a red shift with decreasing cluster size due to the negative Grüneisen parameter along with the contraction of the surface.

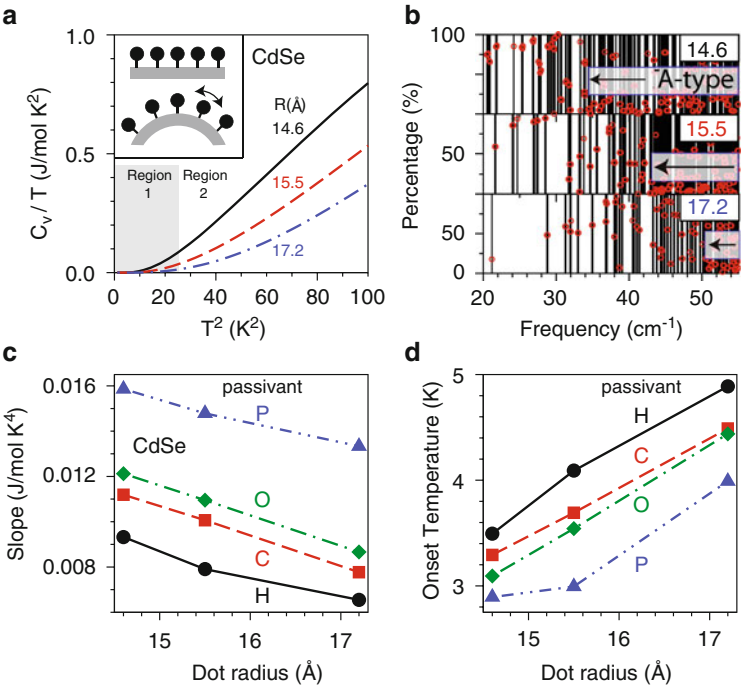

Fig. 7 Specific heat C_v divided by the temperature T as a function of T^2 for different CdSe nanoclusters. In (**b**) the low frequency eigenmodes are drawn as *vertical lines* for three different CdSe nanoclusters. The *solid circle* gives the percentage of surface character of each mode. In (**c**) we estimated the slopes in the (nearly) linear regime of panel (**a**) for CdSe nanoclusters, changing the passivant mass. In (**d**) we report the corresponding onset temperature of C_v

These bulk-like contributions are reflected in the nearly linear behavior in Fig. 7a. We estimated the slopes and the onset temperature of the curves and plotted them in Fig. 7c, d with the passivant mass as hydrogen, carbon, oxygen and phosphorous. The slope reduces with increasing size in all cases and it increases with increasing mass of passivant. This behavior can be understood from the reduced frequency with increasing passivant masses. From Fig. 7d, we find that the smaller nanoclusters have an earlier onset than the larger ones. This is again related to the surface mode softening we reported for decreasing cluster size.

4 Summary

In summary, we have performed ab initio DFT calculations to study the confinement and the surface effects on the vibrational and thermodynamic properties of III–V and II–VI colloidal nanoclusters with up to thousand atoms. We can identify the

following confinement and surface effects. (i) The LA, TO and LO-derived cluster modes of III–V clusters significantly blue shift with decreasing cluster size. For II–VI clusters this shift is absent but the broadening of bulk derived modes is significant and the gap between optical and acoustic phonons is filled by surface modes. (ii) We can clearly ascribe these observations to the large relaxation of the clusters dominated by an inward relaxation of the surface penetrating deep inside the cluster in case of the III–Vs and a large distribution of bond length at the surface of II–VIs. These strong confinement effects tend to disappear for clusters with more than 1,000 atoms. (iii) We find surface optical modes in the phonon gap and surface acoustic modes as the lowest frequency modes. The *coherent acoustic phonons* are identified and found to be in good agreement with results from the Lamb model and experiment. (iv) In the unpassivated nanoclusters, the unpaired electrons in the sp^3 hybrid orbitals reduce the bond strength and result in red shift with frozen geometry. Once the geometry is optimized, the dangling bonds tend to transform from sp^3 to sp^2 hybrid orbitals and leads to a blue shift of vibrational frequencies. (v) The low temperature specific heat reflects the surface acoustic vibrational modes and we suggest to study the low temperature specific heat to access the surface properties.

References

1. Rogach, A. L., Eychmüller, A., Hickey, S. G., Kershaw, S. V.: Infrared-emitting colloidal nanocrystals: Synthesis, assembly, spectroscopy, and applications. Small **3**, 536–557 (2007).
2. Gaponik, N., Hickey, S. G., Dorfs, D., Rogach, A. L., Eychmüller, A.: Progress in the light emission of colloidal semiconductor nanocrystals. Small **6**, 1364–1378 (2010).
3. Talapin, D. V., Lee, J-S., Kovalenko, M. V. Shevchenko, E. V.: Prospects of colloidal nanocrystals for electronic and optoelectronic applications. Chem. Rev. **110**, 389–458 (2010).
4. Fischer, J. Loss, D: Hybridization and spin decoherence in heavy-hole quantum dots. Phys. Rev. Lett. **105**, 266603(4pp) (2010).
5. Kilina, S. V., Kilin, D. S., Prezhdo, O. V.: Breaking the phonon bottleneck in PbSe and CdSe quantum dots: Time-domain Density Functional Theory of charge carrier relaxation. ACS Nano **3**, 93–99 (2009).
6. An, J.M., Califano, M., Franceschetti, A., Zunger, A.: Excited-state relaxation in PbSe quantum dots. J. Chem. Phys. **128**, 164720 (7pp) (2008).
7. Baroni, S., de Gironcoli, S., Corso A. D.: Phonons and related crystal properties from density-functional perturbation theory. Rev. Mod. Phys. **73**, 515–562 (2001).
8. Peelaers, H., Partoens, B., Peeters, F. M.: Phonon Band Structure of Si Nanowires: A Stability Analysis Nano Lett. **9**, 107 (5pp) (2009).
9. Caudal, M., Saitta, A. M., Lazzeri, M., Mauri, F.: Kohn anomalies and nonadiabaticity in doped carbon nanotubes. Phys. Rev. B **75**, 115423 (11pp) (2007).
10. Chelikowsky, J. R., Zayak, A. T., Chan, T., Tiago, M. L., Zhou, Y., Saas, Y.: Algorithms for the electronic and vibrational properties of nanocrystals. J.Phys. Condens. Matter **21**, 064207 (2009).
11. Han, P., Bester, G.: Confinement effects on the vibrational properties of III-V and II-VI nanoclusters. Phys. Rev. B **85**, 041306(R) (4pp) (2012).
12. The CPMD consortium page, coordinated by M. Parrinello and W. Andreoni, Copyright IBM Corp 1990–2008, Copyright MPI für Festkörperforschung Stuttgart 1997–2001 http://www.cpmd.org.

13. Bester, G., Han, P. in: Nagel, W. E., Kröner, D. B., and Resch, M. M., eds. *H*igh Performance Computing in Science and Engineering'11, p.119, Springer-Verlag Berlin Heidelberg 2012.
14. Oron, D., Aharoni, A., de MelloDonega, C., van Rijssel, J., Meijerink, A., Banin, U.: Universal Role of Discrete Acoustic Phonons in the Low-Temperature Optical Emission of Colloidal Quantum Dots. Phys. Rev. Lett. **102**, 177402 (4pp) (2009).
15. Krauss, T. D., Wise, F. W.: Coherent Acoustic Phonons in a Semiconductor Quantum Dot. Phys. Rev. Lett. **79**, 5102 (4pp) (1997).
16. Chilla, G., Kipp, T., Menke, T., Heitmann, D., Nikolic, M., Fromsdorf, A., Kornowski, A., Forster, S., Weller, H.: Direct Observation of Confined Acoustic Phonons in the Photoluminescence Spectra of a Single CdSe-CdS-ZnS Core-Shell-Shell Nanocrystal. Phys. Rev. Lett. **100**, 057403 (4pp) (2008).
17. Tang, J., Kemp, K. W., Hoogland, S., Jeong, K. S., Liu, H., Levina, L., Furukawa, M., Wang, X., Debnath, R., Cha, D., Chou, K. W., Fischer, A., Amassian, A., Asbury, J. B., Sargent, E. H.: Colloidal-quantum-dot photovoltaics using atomic-ligand passivation. Nature materials. **10**, 765 (7pp) (2011).
18. Saviot, L., Champagnon, B., Duval, E., Ekimov, A. I.: Size-selective resonant Raman scattering in CdS doped glasses. Phys. Rev. B **57**, 341 (6pp) (1998).
19. Han, P., Bester, G.: Insights about the surface of colloidal nanoclusters from their vibrational and thermodynamic properties. J. Phys. Chem. C **116**, 10790 (6pp) (2012).